

5 **The terrestrial biosphere and atmosphere interact through a series of feedback**
6 **loops. Variability in terrestrial vegetation growth and phenology can modulate fluxes of**
7 **water and energy to the atmosphere, and thus affect the climatic conditions that in turn**
8 **regulate vegetation dynamics. Here we analyze satellite observations of solar-induced**
9 **fluorescence, precipitation, and radiation using a multivariate statistical technique. We**
10 **find that biosphere-atmosphere feedbacks are globally widespread and regionally**
11 **strong: they explain up to 30% of precipitation and surface radiation variance.**
12 **Substantial biosphere-precipitation feedbacks are often found in regions that are**
13 **transitional between energy and water limitation, such as semi-arid or monsoonal**
14 **regions. Substantial biosphere-radiation feedbacks are often present in several**
15 **moderately wet regions and in the Mediterranean, where precipitation and radiation**
16 **increase vegetation growth. Enhancement of latent and sensible heat transfer from**
17 **vegetation accompanies this growth, which increases boundary layer height and**
18 **convection, affecting cloudiness, and consequently incident surface radiation. Enhanced**
19 **evapotranspiration can increase moist convection, leading to increased precipitation.**
20 **Earth system models underestimate these precipitation and radiation feedbacks mainly**
21 **because they underestimate the biosphere response to radiation and water availability.**
22 **We conclude that biosphere-atmosphere feedbacks cluster in specific climatic regions**
23 **that help determine the net CO₂ balance of the biosphere.**

24 By influencing the partitioning of turbulent fluxes at the surface¹, soil moisture and
25 temperature can affect climatic variability². Biospheric variability, in terms of both
26 phenology and stomatal regulation, also strongly modulates turbulent fluxes of both water
27 and energy³. Since biospheric variability is regulated by vegetation phenology and root zone
28 soil moisture, it exhibits longer (e.g. multi-month) memory compared to the more commonly
29 studied surface soil moisture and temperature state. Therefore, an understanding of

30 biosphere-atmosphere interactions has the potential to improve seasonal to interannual
31 climatic predictions^{4,5,6}, and improve predictions of vegetation resilience to climate
32 anomalies⁷. However, global variations in the strength of biosphere-atmosphere feedbacks
33 remain unknown, in part because of the difficulty of observing biospheric fluxes⁸.

34 Recent advancements in space-borne observations of solar-induced fluorescence (SIF)
35 have enabled for the first-time a global proxy for gross primary productivity (GPP) and
36 vegetation phenology. SIF is a by-product of photosynthesis⁹ related to light-use efficiency
37 (LUE) and to the fraction of absorbed photosynthetic active radiation (fAPAR)¹⁰. On a
38 canopy or regional scale and at a monthly resolution it is nearly proportional to GPP across
39 various ecosystems. This large-scale correspondence is strongly related to the changes in
40 canopy structure and phenology on absorbed photosynthetic active radiation, in addition to
41 the more subtle changes in LUE^{11,12,13,14}. SIF is also generally highly correlated with
42 evapotranspiration (ET)¹⁵ (Supplementary Fig. 1) and correlates with vegetation-driven
43 changes in surface albedo. Here, we use SIF as an integrated measure of vegetation
44 variability, capturing both growth and changes in photosynthetic capacity (Methods).

45 Previous studies of land-atmosphere interactions have typically relied on correlations
46 between land and atmospheric variables^{16,17,18}. However, these variables seasonally coevolve,
47 and thus it is difficult to determine whether one variable is causally forcing the other, or if the
48 two are both driven by separate factors^{19,20}. Here, these shortcomings are overcome by
49 employing a Multivariate Conditional Granger causality (MVGCC) statistical technique using
50 vector autoregressive models (VARs)²¹. This method determines both the strength of the
51 predictive mechanism between variables and the time scale over which these links occur
52 (Methods).

53 **MVGC observational data forcings**

54 We apply the MVGC VAR statistical technique to eight years of monthly SIF
55 measurements from the Global Ozone Monitoring Experiment 2 (GOME-2) sensor²². SIF-
56 precipitation interactions are assessed using remote sensing-based estimates from the Global
57 Precipitation Climatology Project (GPCP)²³ and SIF-radiation interactions are assessed using
58 photosynthetic active radiation (PAR) from Clouds and the Earth's Radiant Energy System
59 (CERES)²⁴. We also use surface air temperature reanalysis data from ERA-Interim²⁵, as
60 temperature can independently impact and interact with photosynthetic activity¹⁸. SIF data is
61 relatively noisy, and thus spatial averaging is used to smooth it prior to analysis (Methods). It
62 should be acknowledged that the smoothing could distort results in highly heterogeneous
63 regions where signals from various biomes may be aggregated. Note that, although the linear
64 scaling factor between monthly SIF and GPP varies between ecosystems and climates¹² the
65 pixel-by-pixel data normalization used here removes the geographical variations of this factor
66 (Methods). The analysis presented here is independent of the scaling factor.

67 To identify biosphere-atmosphere coupled feedbacks, we first examine their
68 directional sub-components, i.e. the *atmospheric forcing* (atmosphere → biosphere), as
69 assessed by the response of SIF (GPP) to atmospheric drivers (the fraction of variance in SIF
70 explained by precipitation and PAR), and the *biospheric forcing* (biosphere → atmosphere),
71 as assessed by precipitation and PAR response to SIF (the fraction of variance in
72 precipitation and PAR explained by SIF) (Fig. 1). An F-test with a null-hypothesis of 0-
73 Granger causality (G-causality) (p-value <0.1) is used. The total feedback strength is then
74 defined as the product of these two directional components (Fig. 2). The sign of the feedback
75 is defined as the sign of the first order coefficient of the VAR model from the G-causality
76 analysis. To ensure the results presented here are robust and independent of the seasonal
77 cycle (i.e. due to land-atmosphere interactions), a bootstrap test that conserves the seasonal

78 cycle but breaks the causality by shuffling months from different years is used
79 (Supplementary Fig. 2) and clearly destroys the feedback.

80 Globally, precipitation positively explains the highest fraction of biosphere (SIF)
81 variability in regions that are transitional between wet and dry climates, e.g. semi-arid or
82 monsoonal (Fig. 1a), consistent with previous studies^{7,16}. Many of these regions also have
83 high fractions of C4 plants²⁶, which have higher water use efficiency than C3 species²⁷, and
84 are therefore expected to be more sensitive to water limitations. The impact of the biosphere
85 on precipitation (Fig. 1b), as assessed by the G-causality of SIF on precipitation, is seen in
86 seasonally dry regions where increases in GPP, in response to increased soil moisture and
87 vegetation growth, is linked with higher latent heat flux and reduced sensible heat flux
88 (Supplementary Fig. 1). Although the impact of SIF on precipitation is less widespread than
89 that of precipitation on SIF, it is significant in many of the same regions. The feedbacks are
90 almost always positive because the monthly positive effect of evapotranspiration on moist
91 convection dominates negative feedback pathways induced by mesoscale surface
92 heterogeneity²⁸ and the effects of changing albedo. The time scales involved in the feedback
93 mechanisms can vary between regions. The subseasonal signal may represent variability due
94 to early greening induced by increased water supply or to browning induced by water stress,
95 while seasonal and interannual signals may indicate changes in vegetation growth regulated
96 by water availability during cell division. The strongest signals are detected subseasonally in
97 monsoonal Australia, seasonally in Eastern Asia, and both seasonally and interannually in the
98 Sahel and Southern African Monsoonal regions (Supplementary Fig. 3). The dominance of
99 seasonal and interannual time scales in the Sahel, related to biomass variability, is consistent
100 with previous understanding^{6,29}.

101 PAR has the greatest impact on biosphere fluxes (Fig. 1c) in regions where
102 photosynthesis and vegetation growth is energy limited such as the high latitudes, humid

103 regions of the Eastern US, parts of the Mediterranean, and tropical rainforest regions^{30,31}.
104 This agrees with the findings of previous studies showing that net primary production (NPP)
105 in these regions is driven by radiation¹⁸. The biosphere exerts control on PAR in the Eastern
106 US, central Eurasia, African deciduous woodlands as well as in the European Mediterranean
107 region (Fig. 1d). In these very dry or very wet regions, ecosystems rarely enter the
108 transitional regime where stomatal closure depends on soil moisture, and increases in SIF are
109 accompanied by increases in both sensible and latent heat (Supplementary Fig. 1)³². The
110 increased sensible heat flux leads to a deeper boundary layer and reduced cloud cover
111 (Supplementary Fig. 4), therefore increasing PAR (Fig. 1d). In the Eastern US, the increase in
112 PAR is mostly attributed to a reduction of low- and mid-level (i.e. congestus) cumulus
113 clouds, typical of summer conditions in this humid climate (Supplementary Fig. 4). By
114 contrast, in the European Mediterranean, PAR is most sensitive to mid- and high-level
115 clouds. In central Eurasia all cloud cover levels negatively impact surface PAR but high-level
116 clouds are the primary reason for the PAR change. The strongest feedbacks between SIF and
117 PAR tend to be on a seasonal scale indicating an increase in ecosystem-scale photosynthetic
118 capacity due to vegetation growth, with exceptions in Madagascar, Australia and central
119 Eurasia where subseasonal and interannual feedbacks dominate (Supplementary Fig. 3). In all
120 PAR feedback regions, PAR is also negatively correlated with precipitation (Supplementary
121 Fig. 4). We note that the European Mediterranean has been highlighted as a hotspot of land-
122 atmosphere coupling in an earlier modeling study, emphasizing the strong coupling between
123 surface turbulent fluxes and the boundary layer response in the region³³. While a similar
124 coupling mechanism may occur in other regions, they do not exhibit a strong response
125 because other processes (e.g. topography, different land-ocean circulation...) overshadow the
126 regional impact of the biosphere there.

127 **MVGC observational data coupled feedbacks**

128 The results of the *atmospheric* and *biospheric forcings* (Fig. 1) are combined to
129 determine the total variance explained in the coupled biosphere-atmosphere system (Fig. 2
130 and Supplementary Fig. 5). Hotspot regions for the precipitation → SIF → precipitation
131 feedback (Fig. 2a) - which can explain up to 20-30% of the observed precipitation variance -
132 are concentrated in grasslands and savannas (transitional zones) such as monsoonal regions in
133 the Sahel, Eastern India and Northern Australia, as well as the African savanna, Madagascar
134 and the Brazilian savannas. There are other monsoonal regions that despite large shifts in
135 rainfall during the year are not hotspots either due to a lack of ET response to precipitation³⁴,
136 or a lack of precipitation response to changes in ET³⁵. An example of this is the Central Great
137 Plains in North America (a hotspot per previous modeling-based studies of soil moisture-
138 atmosphere interactions³⁶), where soil moisture has been shown to have a weak triggering
139 effect on precipitation^{20,37}. Indeed, summertime precipitation in this area is dominated by
140 eastward propagating mesoscale convective systems mostly independent of the land
141 surface³⁸.

142 The PAR → SIF → PAR feedback (Fig. 2b) has hotspots (20-30% of explained
143 variance) in the humid Eastern United States, Southern Brazil, as well as in the
144 Mediterranean basin in Europe. By contrast, in the tropical rainforest regions of Africa and
145 South America there is little response detected for the full feedback loops with either
146 precipitation or PAR (Fig. 2 and Supplementary Fig. 5) suggesting that other factors (such as
147 ecosystem characteristics³⁹) dominate the variability of the biosphere there.

148 Although feedbacks between the biosphere and atmosphere are detected in almost all
149 regions, several 'hotspot families' stand out: 1) regions that are either semi-arid or monsoonal
150 for the precipitation feedback and 2) humid regions (the Eastern US) and the Mediterranean

151 for the PAR feedback. No regions exhibit both feedback pathways; one always dominates the
152 other when it is present.

153 **MVGC ESM analysis**

154 The distribution of feedbacks in the observational record is next used to assess Earth
155 System Models (ESMs) (Supplementary Table 1). The distributions of feedback strengths for
156 model and observational results (Fig. 3) summarize the differences between the biosphere-
157 atmosphere feedback detected by each CMIP5 model (Supplementary Figs 6, 7 and 8) and
158 the observational record. In the model analysis, GPP is used as a proxy for the biosphere in
159 lieu of SIF. Our results are normalized in terms of explained variance for each pixel so that
160 the proportionality factor of SIF and GPP does not impact the pixel-wise metric results. To
161 increase robustness, 50 years of data are used for the model analysis (1956-2005) rather than
162 the shorter period we are constrained by for the observational analysis⁴⁰.

163 The median of all ESMs fall below the first quartile of the observational data results
164 for the precipitation → biosphere → precipitation feedback (Fig. 3a). Models significantly
165 underestimate the magnitude and the range of both the *atmospheric* and *biospheric forcings*
166 (except for CMCC-CESM) (Supplementary Fig. 6), although underestimation is more severe
167 in the case of the precipitation → biosphere component. The observational PAR → biosphere
168 → PAR feedback strength (Fig. 3b) also has a higher median value than that of the ESMs.
169 Both the precipitation and PAR *atmospheric forcings* are underestimated because of
170 photosynthesis misrepresentation in ESMs (Supplementary Fig. 6)⁴¹. Despite some spatial
171 similarities between modeled feedbacks and observational results (Supplementary Figs 7 and
172 8), models systematically underestimate the impact of the biosphere on precipitation, and
173 noticeably miss the variance explained by observations in monsoonal Australia. On the other
174 hand, the modeled impact of the biosphere on PAR varies drastically between models and can

175 be either over- or under-estimated (Supplementary Fig. 6). These inter-model discrepancies
176 are likely due to the misrepresentation of convection in models, and the challenges of
177 correctly representing it over land regions^{42,43}. Interestingly, in general, ESM errors in
178 representing the atmospheric forcing on the biosphere are even more severe than errors in
179 representing the biospheric forcing on the atmosphere. This suggests that better
180 representations of photosynthesis and water stress sensitivities would have a larger impact on
181 improving the ESM representation of biosphere-atmosphere feedbacks, than improved
182 convection representation.

183 This study provides the first causal observational diagnostic of biosphere-atmosphere
184 feedbacks on subseasonal to interannual time scales. These feedbacks are strong in semi-arid
185 and monsoonal regions, which are key in determining whether the yearly global terrestrial
186 biosphere acts as a net CO₂ source or sink^{7,16}. As such biosphere-atmosphere feedbacks
187 regulate interannual hydrology and climate in these regions as well as the global carbon
188 cycle. Additionally, due to the high percentages of atmospheric variability explained by
189 vegetation processes, subseasonal and seasonal climate predictions can greatly benefit from
190 better vegetation characterization in ESMs. In turn this will improve subseasonal to seasonal
191 climate and hydrologic forecasts, which are crucial for optimizing management decisions
192 pertaining to food security, water supplies, and disaster management such as droughts and
193 heat waves.

194 **Main Text References**

- 195 1. Bateni, S. M. & Entekhabi, D. Relative efficiency of land surface energy balance
196 components. *Water Resour. Res.* **48**, 1–8 (2012).
- 197 2. Koster, R. D., Suarez, M. J. & Heiser, M. Variance and Predictability of Precipitation
198 at Seasonal-to-Interannual Timescales. *J. Hydrometeorol.* **1**, 26–46 (2000).
- 199 3. van den Hurk, B. J. J. M., Viterbo, P. & Los, S. O. Impact of leaf area index
200 seasonality on the annual land surface evaporation in a global circulation model. *J.*
201 *Geophys. Res.* **108**, 5.1-5.7 (2003).
- 202 4. Guo, Z., Dirmeyer, P. A., Delsole, T. & Koster, R. D. Rebound in atmospheric
203 predictability and the role of the land surface. *J. Clim.* **25**, 4744–4749 (2012).
- 204 5. Koster, R. D. *et al.* The Second Phase of the Global Land–Atmosphere Coupling
205 Experiment: Soil Moisture Contributions to Subseasonal Forecast Skill. *J.*
206 *Hydrometeorol.* **12**, 805–822 (2011).
- 207 6. Zeng, N., Neelin, J., Lau, K. & Tucker, C. Enhancement of Interdecadal Climate
208 Variability in the Sahel by Vegetation Interaction. *Science* **286**, 1537–1540 (1999).
- 209 7. Poulter, B. *et al.* Contribution of semi-arid ecosystems to interannual variability of the
210 global carbon cycle. *Nature* **509**, 600–603 (2014).
- 211 8. Koster, R. D. *et al.* On the nature of soil moisture in land surface models. *J. Clim.* **22**,
212 4322–4335 (2009).
- 213 9. Porcar-Castell, A. *et al.* Linking chlorophyll a fluorescence to photosynthesis for
214 remote sensing applications: Mechanisms and challenges. *J. Exp. Bot.* **65**, 4065–4095
215 (2014).

- 216 10. Guanter, L. *et al.* Global and time-resolved monitoring of crop photosynthesis with
217 chlorophyll fluorescence. *Proc. Natl. Acad. Sci. U. S. A.* **111**, E1327-33 (2014).
- 218 11. Zhang, Y. *et al.* Remote Sensing of Environment Consistency between sun-induced
219 chlorophyll fluorescence and gross primary production of vegetation in North
220 America. *Remote Sens. Environ.* **183**, 154–169 (2016).
- 221 12. Frankenberg, C. *et al.* New global observations of the terrestrial carbon cycle from
222 GOSAT: Patterns of plant fluorescence with gross primary productivity. *Geophys. Res.*
223 *Lett.* **38**, L17706 (2011).
- 224 13. Frankenberg, C., O’Dell, C., Guanter, L. & McDuffie, J. Remote sensing of near-
225 infrared chlorophyll fluorescence from space in scattering atmospheres: Implications
226 for its retrieval and interferences with atmospheric CO₂ retrievals. *Atmos. Meas.*
227 *Tech.* **5**, 2081–2094 (2012).
- 228 14. Wood, J. D. *et al.* Multi-scale analyses reveal robust relationships between gross
229 primary production and solar induced fluorescence. *Geophys. Res. Lett.* **In Review**,
230 533–541 (2016).
- 231 15. Schlesinger, W. H. & Jasechko, S. Transpiration in the global water cycle. *Agric. For.*
232 *Meteorol.* **189–190**, 115–117 (2014).
- 233 16. Ahlström, A. *et al.* The dominant role of semi-arid ecosystems in the trend and
234 variability of the land CO₂ sink. *Science (80-.).* **348**, 895–899 (2015).
- 235 17. Beer, C. *et al.* Terrestrial gross carbon dioxide uptake: global distribution and
236 covariation with climate. *Science* **329**, 834–838 (2010).
- 237 18. Nemani, R. R. *et al.* Climate-driven increases in global terrestrial net primary
238 production from 1982 to 1999. *Science* **300**, 1560–1563 (2003).

- 239 19. Sugihara, G. *et al.* Detecting causality in complex ecosystems. *Science* **338**, 496–500
240 (2012).
- 241 20. Tuttle, S. & Salvucci, G. Empirical evidence of contrasting soil moisture–precipitation
242 feedbacks across the United States. **352**, 825–828 (2016).
- 243 21. Barnett, L. & Seth, A. K. The MVGC multivariate Granger causality toolbox: A new
244 approach to Granger-causal inference. *J. Neurosci. Methods* **223**, 50–68 (2014).
- 245 22. Joiner, J. *et al.* Global monitoring of terrestrial chlorophyll fluorescence from
246 moderate spectral resolution near-infrared satellite measurements: methodology,
247 simulations, and application to GOME-2. *Atmos. Meas. Tech. Discuss.* **6**, 3883–3930
248 (2013).
- 249 23. Pendergrass, A. & N. C. for A. R. S. (Eds). The Climate Data Guide: GPCP
250 (Monthly): Global Precipitation Climatology Project. 1–2 (2016). Available at:
251 [https://climatedataguide.ucar.edu/climate-data/gpcp-monthly-global-precipitation-](https://climatedataguide.ucar.edu/climate-data/gpcp-monthly-global-precipitation-climatology-project)
252 [climatology-project](https://climatedataguide.ucar.edu/climate-data/gpcp-monthly-global-precipitation-climatology-project).
- 253 24. Wielicki, B. A. *et al.* Clouds and the Earth’s Radiant Energy System (CERES): An
254 Earth Observing System Experiment. *Bull. Amer. Meteor. Soc.* **77**, 853–868 (1996).
- 255 25. Dee, D. P. *et al.* The ERA-Interim reanalysis: Configuration and performance of the
256 data assimilation system. *Q. J. R. Meteorol. Soc.* **137**, 553–597 (2011).
- 257 26. Still, C. J., Berry, J. A., Collatz, G. J. & DeFries, R. S. Global distribution of C 3 and
258 C 4 vegetation: Carbon cycle implications. *Global Biogeochem. Cycles* **17**, 6-1-6–14
259 (2003).
- 260 27. Ghannoum, O. C4 photosynthesis and water stress. *Ann. Bot.* **103**, 635–644 (2009).
- 261 28. Guillod, Benoit P. (Institute for Atmospheric and Climate Science, Department of

- 262 Environmental Systems Science, E. Z., Orlowsky, B., Miralles, D. G., Teuling, A. J. &
263 Seneviratne, S. I. Reconciling spatial and temporal soil moisture effects on afternoon
264 rainfall. *Nat. Commun.* **6**, 6443 (2015).
- 265 29. Charney, J. G. Dynamics of deserts and drought in the Sahel. *Q. J. R. Meteorol. Soc.*
266 **101**, 193–202 (1975).
- 267 30. Anber, U., Gentine, P., Wang, S. & Sobel, A. H. Fog and rain in the Amazon. *Proc.*
268 *Natl. Acad. Sci.* **112**, 11473–11477 (2015).
- 269 31. Brando, P. M. *et al.* Seasonal and interannual variability of climate and vegetation
270 indices across the Amazon. *Proc. Natl. Acad. Sci. U. S. A.* **107**, 14685–90 (2010).
- 271 32. Seneviratne, S. I. *et al.* Investigating soil moisture-climate interactions in a changing
272 climate: A review. *Earth-Science Rev.* **99**, 125–161 (2010).
- 273 33. Seneviratne, S. I., Lüthi, D., Litschi, M. & Schär, C. Land-atmosphere coupling and
274 climate change in Europe. *Nature* **443**, 205–209 (2006).
- 275 34. Dirmeyer, P. A. The terrestrial segment of soil moisture-climate coupling. *Geophys.*
276 *Res. Lett.* **38**, L16702 (2011).
- 277 35. Koster, R. D. & Suarez, M. J. Impact of Land Surface Initialization on Seasonal
278 Precipitation and Temperature Prediction. *J. Hydrometeorol.* **4**, 408–423 (2003).
- 279 36. Koster, R. D. *et al.* GLACE: The Global Land – Atmosphere Coupling Experiment.
280 Part I: Overview. *J. Hydrometeorol.* **7**, 611–625 (2006).
- 281 37. Findell, K. L., Gentine, P., Lintner, B. R. & Kerr, C. Probability of afternoon
282 precipitation in eastern United States and Mexico enhanced by high evaporation. *Nat.*
283 *Geosci.* **4**, 434–439 (2011).
- 284 38. Storer, R. L., Zhang, G. J. & Song, X. Effects of convective microphysics

- 285 parameterization on large-scale cloud hydrological cycle and radiative budget in
286 tropical and midlatitude convective regions. *J. Clim.* **28**, 9277–9297 (2015).
- 287 39. Levine, N. M. *et al.* Ecosystem heterogeneity determines the ecological resilience of
288 the Amazon to climate change. *Proc. Natl. Acad. Sci.* (2015).
289 doi:10.1073/pnas.1511344112
- 290 40. Findell, K. L., Gentine, P., Lintner, B. R. & Guillod, B. P. Data Length Requirements
291 for Observational Estimates of Land–Atmosphere Coupling Strength. *J.*
292 *Hydrometeorol.* **16**, 1615–1635 (2015).
- 293 41. Zhou, S., Duursma, R. A., Medlyn, B. E., Kelly, J. W. G. & Prentice, I. C. How should
294 we model plant responses to drought? An analysis of stomatal and non-stomatal
295 responses to water stress. *Agric. For. Meteorol.* **182–183**, 204–214 (2013).
- 296 42. Bony, S. *et al.* Clouds, circulation and climate sensitivity. *Nat. Geosci.* **8**, 261–268
297 (2015).
- 298 43. Zhao, M. *et al.* Uncertainty in model climate sensitivity traced to representations of
299 cumulus precipitation microphysics. *J. Clim.* **29**, 543–560 (2016).
- 300

301 **Corresponding author**

302 Correspondence and requests for materials should be addressed to JKG
303 (jg3405@columbia.edu).

304 **Acknowledgements**

305 The authors would like to thank Guido Salvucci and Upmanu Lall for discussion on
306 the Granger causality, Randal Koster for initial discussion of the paper, and Joanna Joiner for
307 providing GOME-2 data. This project was supported by both a NASA Earth Science and
308 Space Fellowship as well as a DOE GOAmazon grant.

309 “We acknowledge the World Climate Research Programme's Working Group on
310 Coupled Modelling, which is responsible for CMIP, and we thank the climate modeling
311 groups (listed in Table S1 of this paper) for producing and making available their model
312 output. For CMIP the U.S. Department of Energy's Program for Climate Model Diagnosis
313 and Intercomparison provides coordinating support and led development of software
314 infrastructure in partnership with the Global Organization for Earth System Science Portals.”

315 **Author Contributions**

316 JKG, AGK and PG wrote the main manuscript text. JKG, PG and SHA prepared
317 figures. SHA processed the CMIP5 simulations. JKG, PG and AGK designed the study. All
318 authors reviewed and edited the manuscript.

319 **Reprints and permissions**

320 Reprints and permissions information is available at www.nature.com/reprints.

321 **Competing financial interests**

322 The authors declare no competing financial interests.

323 **Figure Captions**

324 **Figure 1. Atmospheric forcings and biospheric forcings.** $X \rightarrow Y$ represents the fraction of
325 variance of Y explained by X, for the *atmospheric forcing* (atmosphere \rightarrow biosphere) (**a,c**),
326 and *biospheric forcing* (biosphere \rightarrow atmosphere) (**b,d**). The signs of the fractions in the top
327 row show whether the atmospheric variable increases (positive) or decreases (negative) the
328 biosphere flux, while in the bottom row they show whether the biosphere increases or
329 decreases the atmospheric response. Oceans and regions where SIF partial correlations are
330 less than 0.1 are shown in white. Pixels without significance are shown in gray (p-value<0.1).
331

332 **Fig. 2. Hotspots of terrestrial biosphere-atmosphere feedbacks.** The fraction of biosphere-
333 atmosphere coupling variance explained for the full feedback loop: precipitation \rightarrow SIF \rightarrow
334 precipitation (**a**) and PAR \rightarrow SIF \rightarrow PAR (**b**). The sign of the fraction shows whether the
335 feedback is positive or negative. Oceans and regions where SIF partial correlations are less
336 than 0.1 are shown in white. Pixels without significance are shown in gray (p-value<0.1).

337

338 **Fig. 3. Comparison of observational and Earth System Model results.** Boxplots showing
339 the distributions of significant observational and model results for the fractions of variance
340 explained for the feedbacks of precipitation \rightarrow biosphere \rightarrow precipitation (**a**) and PAR \rightarrow
341 biosphere \rightarrow PAR (**b**). Boxes are defined by the upper quartile, median and lower quartile of
342 the data while whiskers are defined by the outliers. Only significant pixels are represented (p-
343 value<0.1).

344

345

346 **Methods**

347 **Datasets**

348 Observational remote sensing data is used for SIF, precipitation, and PAR, while
349 quasi-observational reanalysis data is used for temperature. GOME-2, version 2.6²² (overpass
350 time of 9:30am) is used for SIF, precipitation data is obtained from version 1.2 of GPCP²³,
351 PAR from CERES²⁴, and surface air temperature (1000mb) data from ERA-Interim²⁵ (see
352 Data availability). While a longer observational data record would allow further insight into
353 interannual variability, we are limited by the satellite data record availability.

354 There is a certain amount of uncertainty inherent to each product that is described in
355 detail in their data quality summaries. The SIF data is especially noisy (particularly in South
356 America where there are less frequent measurements due to clouds, specifically in the
357 rainforest, and noise from the South Atlantic Anomaly)²². Thus, in addition to a standard
358 normalization (described below), SIF data is averaged with the 8 adjacent pixels surrounding
359 the pixel of interest to smooth the remaining noise. On rare pixels, we note that SIF appears
360 to cause an increase in both precipitation and PAR (Figs 1b and d) but this effect is attributed
361 to the use of nine-pixels spatially smoothing of the SIF signal.

362 The monthly SIF data is calculated from daily measurements (level 2) when the
363 effective cloud fraction is <30%. It should be noted that effective cloud fraction is not
364 equivalent to geometric cloud fraction but is instead based on a Lambertian model that
365 considers cloud reflectance and albedo^{44,45,46}. It has been demonstrated that in a typical pixel
366 with a true cloud fraction of 40% that over 80% of the SIF signal can still be retrieved for
367 very thick cloud optical thicknesses (up to 10)⁴⁷. The effective cloud fraction is typically
368 lower than the geometric one.

369 While cloud filtering could result in a slight bias, it has been shown that altering the
370 effective cloud fraction threshold between 0 and 50 percent only minimally affects the spatial
371 and temporal patterns of SIF²². Therefore, we expect minimal bias due to the filtering at the
372 monthly resolution that we consider in our analysis. The one region where the cloud coverage
373 filtering may reduce G-causality detected is in the wet tropics where there is a higher
374 prevalence of clouds. It is possible that the PAR → SIF → PAR feedbacks might be
375 underestimated in this region because of the cloud contamination.

376 **SIF-GPP relationship**

377 This study uses SIF as a proxy for GPP. SIF is mechanistically linked to GPP^{9,48},
378 through both light use efficiency and fAPAR⁴⁹, and has been shown to have a near-linear
379 relationship with GPP at both canopy and ecosystem scales^{11,12,50,51,46,52}. While the hourly
380 leaf-level relationship between SIF and GPP has been estimated as curvilinear (SIF continues
381 to increase after the maximum rate of photosynthesis has been reached)¹¹, the relationship at
382 larger and longer time scales (e.g., monthly) becomes linear likely due to the effects of
383 averaging across a canopy of leaves representing varying light conditions¹¹.

384 The linearity between SIF and GPP has been observed across biomes using a variety
385 of datasets, including flux tower validation^{46,52}. As is shown in Supplementary Fig. 1, SIF
386 correlates strongly with monthly global GPP estimates from Fluxnet-MTE in regions outside
387 of the wet tropics. The SIF-GPP correlation is lower in the wet tropics as the machine
388 learning upscaling approach of the Fluxnet-MTE GPP product has the greatest uncertainty in
389 these regions, as there are few(er) eddy covariance towers there that are used for training^{53,54}.
390 Additionally, tropical forest GPP exhibits minimal seasonality⁵⁵, and thus the lower
391 correlation can be attributed to the fitting of noise (R^2 by construction will be small). It has
392 nonetheless been shown that the minimal seasonality in SIF observed in the Amazon

393 correctly corresponds to the seasonality of carbon dioxide⁵⁶ and MODIS near-infrared
394 reflectance related to photosynthesis⁵⁵. As a result, SIF has been used as a proxy for GPP
395 interannual variability¹¹.

396 The linear scaling factor between SIF and GPP varies spatially. Yet, when we
397 normalize the data prior to running the G-Causality, the differing slope values should not
398 impact results since we look at each pixel (location/ecosystem) separately.

399 **Conditional MVGC**

400 We base our analysis on Multivariate Granger causality, using a MVGC MATLAB
401 toolbox²¹, which allows for time and frequency domain MVGC analysis of time series data.
402 The method fits multivariate VAR models to time series. Conditional MVGC compares VAR
403 models with and without (potentially causal) variables. For example, if the addition of past
404 values of precipitation improves the quality of the VAR model prediction for SIF (that uses
405 the autoregressive histories of other variables: SIF, PAR and temperature), then precipitation
406 is considered to have a G-causal influence⁵⁷. If there is no significant information gained
407 (based on an F-test with a null-hypothesis of no G-causality), then the variables are
408 considered not to have a causal link.

409 Prior to applying the MVGC technique, the data obtained are aggregated to 1-degree
410 by 1-degree monthly data. Monthly data are used to reduce random noise in the original SIF
411 daily data and to achieve consistency with the monthly-aggregated resolution of Coupled
412 Model Intercomparison Project Phase 5 (CMIP5) model data. For each dataset, the long-term
413 mean value is subtracted from each pixel and it is normalized by its long-term standard
414 deviation. After normalization, SIF data is averaged with the 8 adjacent pixels surrounding
415 the pixel of interest to smooth the remaining noise inherent in the SIF data from GOME-2.
416 Single missing monthly values (approximately 4% of the pixels per month) are interpolated

417 using temporal splines. Prior to performing the normalization and running the MVGC
418 analysis, partial correlations are calculated between non-normalized SIF and atmospheric
419 variables, and if the absolute correlation falls below a value of 0.1, the atmospheric variable
420 is considered non-significant for that pixel and is not included in the analysis. Although
421 results of the analysis are not shown for surface air temperature (temperature at 1000mb), it is
422 used in the analysis, to account for its influence when determining the feedbacks involving
423 precipitation, PAR and SIF. For example, by including temperature in the analysis we
424 guarantee that the G-causality between PAR and SIF is not instead a reflection of the effects
425 of temperature (or related to vapor pressure deficit), which can be correlated with PAR. For
426 all analyses, we use a conservative p-value calculation given the high auto-correlation in the
427 variables of interest, which reduces the degrees of freedom in the number of samples.

428 Note that we intentionally do not remove the seasonal cycle in pre-processing. Small
429 stochastic amplitude and phase modulations of the seasonality (e.g. large monthly cloud
430 cover or colder than usual temperatures in a particular year) induce non-additive widening of
431 the amplitude and phase spectra so that subtracting the climatology artificially reduces
432 specific frequencies and phases, potentially removing part of the causal signal. This risk is
433 amplified by the relatively short remote sensing record used, which could lead to an
434 imperfect definition of the climatological seasonal cycle. Indeed, where the seasonal signal
435 amplitude and phase have a causal effect we want to capture this (such as the rainfall impact
436 on vegetation green-up and SIF in monsoonal regions). Because the VAR models can capture
437 seasonal periodicity, the MVGC analysis is not affected by the risk of false attribution of
438 causality due to simple lagged seasonality, as is further demonstrates in the examples below.

439 After normalization of the data and checking that partial correlations between SIF and
440 the other variables fall above 0.1, the Akaike information criterion is calculated and defines
441 the best model order up to the maximum model order, specified as 6 months

442 ('tsdata_to_infocrit.m' function in the MVGC MATLAB toolbox). The best actual model
 443 order used displays the memory of the biosphere-atmosphere interactions (Supplementary
 444 Fig. 9): model orders of 1 correspond to regions where memory in the system is short and
 445 causal influence between the atmosphere and biosphere is weak. Using the calculated model
 446 order, an ordinary least-square regression is used to determine the multivariate-VAR model
 447 coefficients ('tsdata_to_var.m'). The autocovariance function is created
 448 ('var_to_autocov.m'), and from this we calculate the time domain pair-wise conditional
 449 causalities ('autocov_to_pwcgc.m'). To test time-domain significance, we calculate the p-
 450 values, which are compared to our chosen p-value of less than 0.1 ('mvgc_pval.m'). An F-
 451 test with a null-hypothesis of no G-causality is used and only significant pixels are displayed
 452 in figures. To perform the analysis in the frequency domain and identify subseasonal (<3
 453 months), seasonal (3 to 12 months) and interannual (>1 year) feedbacks, we calculate the
 454 spectral-conditional G-causality ('autocov_to_spwcgc.m') (Supplementary Fig. 3).

455 We check that the G-causality in the frequency domain integrates to the time domain
 456 by integrating the frequency results ('smvgc_to_mvgc.m') and then subtracting the output
 457 from the time domain result. Checks are performed throughout the process so that the
 458 analysis is automatically exited should there be a failed calculation.

459 A sample first order VAR model to explain the variability of SIF is displayed in
 460 equation 1 with A , P , T and sig representing the VAR coefficient matrix, precipitation,
 461 temperature, and significance (1 for significant, 0 for insignificant at $p < 0.1$) accordingly.

$$\begin{aligned}
 SIF(t) = & A_{(SIF)} SIF_{(t-1)} + A_{(P \text{ on } SIF)} P_{(t-1)} sig_{(P \text{ on } SIF)} \\
 & + A_{(PAR \text{ on } SIF)} PAR_{(t-1)} sig_{(PAR \text{ on } SIF)} \\
 & + A_{(T \text{ on } SIF)} T_{(t-1)} sig_{(T \text{ on } SIF)} + \varepsilon
 \end{aligned} \tag{1}$$

462 With the addition of the auto-regressive histories of each variable, the VAR model
 463 captures the original SIF data more accurately. We acknowledge that other factors not
 464 included in this analysis can affect SIF variability (such as naturally and anthropogenically
 465 caused disturbances), and is one of the reasons (along with sensor noise) that we cannot
 466 predict 100% of the variable variance, even with our full VAR model.

467 **Synthetic Bootstrap Tests**

468 To demonstrate the effectiveness of this method, we perform several additional tests
 469 of the conditional MVGC on synthetic data where causal links can be specified. In the first
 470 three test scenarios PAR and precipitation (P) time series are assumed to be sinusoidal with
 471 amplitude modulation – AM – and frequency modulation – FM –, as well as additive noise
 472 (equations 2 and 3). We define two similar test cases except that one has a causal link
 473 (equation 4) while the other does not (non-causal) (equation 5). We assume that the noise is
 474 normally distributed (and thus have a white noise/flat spectrum in the frequency domain). To
 475 test the frequency response, PAR is assumed to have a yearly frequency
 476 $\omega = 2\pi / (12 \text{ months})$ (equation 2) while precipitation is assumed to have twice-yearly
 477 frequency 2ω (i.e. two wet/dry seasons per year) (equation 3).

$$PAR(t) = 100(1 + 0.25A_t^{PAR}) \sin\left(\left(1 + \frac{1}{24}F_t^{PAR}\right)\omega t - \pi/2\right) + 25\varepsilon_t^{PAR} \quad (2)$$

$$P(t) = 100(1 + 0.25A_t^P) \sin\left(\left(1 + \frac{1}{24}F_t^P\right)2\omega t - \pi/4\right) + 25\varepsilon_t^P \quad (3)$$

478 with A_t^{PAR} , F_t^{PAR} , ε_t^{PAR} , A_t^P , F_t^P , ε_t^P i.i.d. normally distributed with unit variance $N(0,1)$.

479 In the *causal case*, SIF is defined as a lagged version of precipitation and radiation
 480 (with t in months) (equation 4):

$$SIF = 0.2(1 + 0.25A_t^{SIF})P(t-2) + 0.8(1 + 0.25B_t^{SIF})PAR(t-1) + 25\epsilon_t^{SIF} \quad (4)$$

481 with $A_t^{SIF}, B_t^{SIF}, \epsilon_t^{SIF}$ i.i.d. normally distributed with unit variance $N(0,1)$. We use 50 years of
 482 synthetic data and one realization for the test.

483 The conditional G-causality finds that only radiation and precipitation are causing SIF
 484 and not the converse (Supplementary Fig. 10). In addition, the magnitude of radiation on SIF
 485 is four times stronger than the one of precipitation on SIF, as expected based on the time
 486 series generated (equation 4).

487 To emphasize that these results are not spurious, we perform a second, similar test but
 488 with a *non-causal* time series (equation 5). This non-casual SIF time series is not induced by
 489 PAR nor precipitation. It is statistically similar to the causal scenario, composed of lagged
 490 sinusoids with similar frequencies to PAR and precipitation, but without a causal mechanism.
 491 For the precipitation and radiation time series we allow for both amplitude and frequency
 492 modulations so that both amplitude and phase are stochastic (similar to radiation and
 493 precipitation monthly time series).

$$\begin{aligned} SIF = & 20(1 + 0.25a_t^{SIF})\sin\left(\left(1 + \frac{1}{24}b_t^{SIF}\right)2\omega t - \pi/2 - (2/12)2\pi\right) \\ & + 80(1 + 0.25c_t^{SIF})\sin\left(\left(1 + \frac{1}{24}d_t^{SIF}\right)\omega t - \pi/4 - (1/12)2\pi\right) \\ & + 25e_t^{SIF} \end{aligned} \quad (5)$$

494 The conditional MVGC analysis of this non-causal time series shows no significant G-
 495 causality, as expected (Supplementary Fig. 10).

496 In the third test we bootstrap every month of equations 2-4 across years, clearly
 497 destroying the causality in the time series (as the same month from another year is used)
 498 while preserving the climatology (and seasonal cycle). As seen in Supplementary Figure 10,

499 the test again finds no causality in the time series, further confirming the quality of the
500 method and its applicability for our type of time series.

501 In a fourth and final synthetic data analysis, we test whether we can detect a *causal*
502 full-feedback loop. We repeat the original *causal* test (equation 4), switching the original
503 equation for PAR (equation 2) for one that also includes SIF as a driver (equation 6).

$$PAR = PAR + 0.4 SIF \text{ var}(PAR)/\text{var}(SIF). \quad (6)$$

504 As expected, in addition to the causality detected previously in the *causal* test of precipitation
505 and PAR on SIF, we also detect significant causality of SIF on PAR (Supplementary Fig. 10).

506 **Observational Bootstrap Test**

507 To further test the assumption that the observed causation of the biosphere on the
508 atmosphere is not an artifact of the seasonal cycle, we perform a bootstrap analysis with 100-
509 realizations at the global scale. Observational data is sampled by randomly swapping the
510 same months across years for each variable: that is the seasonality is preserved while the
511 causal link from month to month is destroyed. As expected, very few pixels showed any G-
512 causality (Supplementary Fig. 2): only 6.2% of the SIF → precipitation results, and 6.9% of
513 the SIF → PAR results were found to be significant at the 95% confidence level (had more
514 than 5/100 realizations per pixel with significant results based on an F-distribution with a p-
515 value < 0.1). The resulting averaged pair-wise conditional G-causality shows almost no
516 signal, with a peak of less than 0.05 compared to 0.3 for the original dataset (Supplementary
517 Fig. 2). In addition, the resulting geographical patterns reflect mostly random noise. This
518 further emphasizes the physical nature of our assessed causation between the biosphere and
519 the atmosphere.

520 **Vector Autoregressive Models**

521 The VAR models obtained from the G-causality analysis are used to quantify the
 522 fraction of variance in the biosphere explained by the atmosphere and vice versa. We tested
 523 for normality and homoscedasticity of the residuals during the VAR fits and excluded pixels
 524 that did not meet these criteria (3-6% of pixels depending on the feedback). Using the VAR
 525 coefficients generated by the analysis (to account for cross variations), VAR models are
 526 created for each atmospheric variable with and without the inclusion of SIF. VAR models are
 527 also created for SIF with and without the inclusion of each atmospheric variable. The
 528 fractions of observed SIF variance explained by each atmospheric component is computed
 529 (equation 7):

$$f_{X \rightarrow SIF} = \frac{\text{var}(SIF_{AR \text{ fit with } X}) - \text{var}(SIF_{AR \text{ fit without } X})}{\text{var}(SIF)} \quad (7)$$

530
 531 as well as the fraction of each atmospheric variable observed variance explained by SIF
 532 (equation 8) (Fig. 1):

$$f_{SIF \rightarrow Y} = \frac{\text{var}(Y_{AR \text{ fit with } SIF}) - \text{var}(Y_{AR \text{ fit without } SIF})}{\text{var}(Y)} \quad (8)$$

533 These are combined to obtain the full feedback fractions (equation 9) (Fig. 2 and
 534 Supplementary Fig. 5):

$$f_{X \rightarrow SIF \rightarrow Y} = \frac{\text{var}(SIF_{AR \text{ fit with } X}) - \text{var}(SIF_{AR \text{ fit without } X})}{\text{var}(SIF)} \times \frac{\text{var}(Y_{AR \text{ fit with } SIF}) - \text{var}(Y_{AR \text{ fit without } SIF})}{\text{var}(Y)} \quad (9)$$

535 The feedback is defined as positive or negative by taking the VAR model first order
 536 coefficients, which is then compared with the VAR model coefficient with the greatest
 537 absolute magnitude as further verification. The leading order coefficient of the AR model

538 could be used in lieu of the first order one but given the rapid decay of the autocorrelation
539 function and the reduced VAR model order (typically less than 2, Supplementary Fig. 9) we
540 use the sign of the first order coefficient. The two estimates of the sign differ in limited
541 regions.

542 **CMIP5 Model Simulations**

543 For the Earth System models from the CMIP5 collection (Supplementary Table 1),
544 the same analysis used for the observational data is applied. Only those models that included
545 GPP data are used. The time period of 1956-2005 is used to obtain statistics that are robust
546 across interannual variability⁴⁰. The true feedback strengths have likely not changed
547 significantly from this earlier, longer time period and the period used for the observational
548 analysis, but we acknowledge that land-use and land-cover changes can affect the feedback
549 metrics (but are also model dependent). One realization of the historical run was used for
550 each model⁵⁸.

551 VAR models are created based on coefficients calculated in the MVGC analysis for
552 each ESM, and the fraction of variance explained in biosphere-atmosphere coupling from
553 each variable is calculated using equations 5-7.

554 **Code availability**

555 The code used as the basis for the study can be accessed from
556 <http://www.sussex.ac.uk/sackler/mvgc/>.

557 **Data availability**

558 All data supporting the findings of this study are freely available from the following
559 locations:

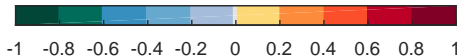
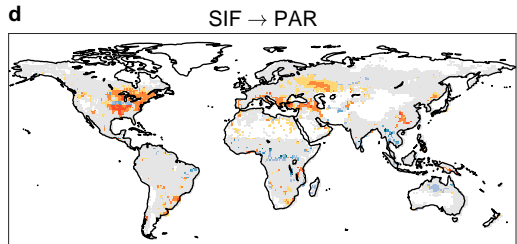
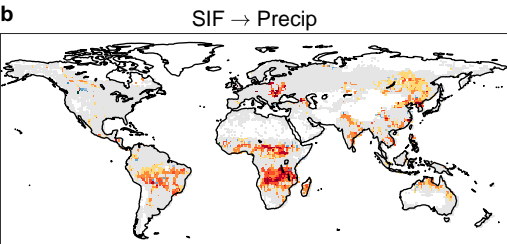
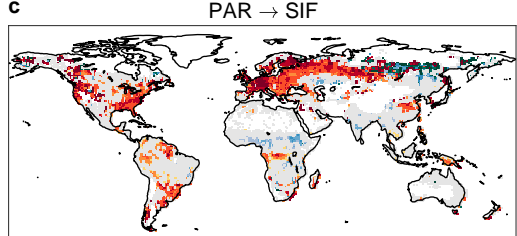
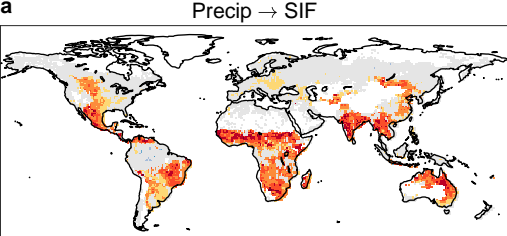
- 560 • GOME-2 SIF: https://avdc.gsfc.nasa.gov/pub/data/satellite/MetOp/GOME_F/

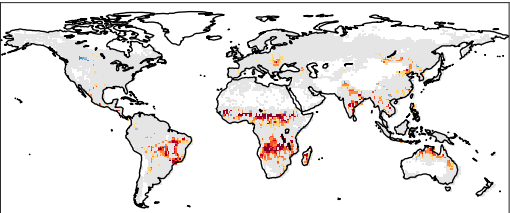
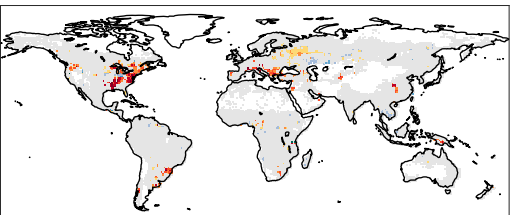
- 561 • GPCP precipitation:
562 <http://iridl.ldeo.columbia.edu/SOURCES/.NASA/.GPCP/.V1DD/.V1p2/>
- 563 • CERES PAR: <https://ceres-tool.larc.nasa.gov/ord-tool/jsp/SYN1degSelection.jsp>
- 564 • CERES cloud coverage:
565 <https://ceres-tool.larc.nasa.gov/ord-tool/jsp/ISCCP-D2Selection.jsp>
- 566 • ERA-Interim temperature and boundary layer height:
567 <http://apps.ecmwf.int/datasets/data/interim-full-mnth/levtype=sfc/>
- 568 • Fluxnet-MTE surface flux and GPP data:
569 <https://www.bgc-jena.mpg.de/geodb/projects/Data.php>
- 570 • CMIP5 model data: <https://pcmdi.llnl.gov/>
- 571 Additional intermediate datasets produced as part of the study can be made available
572 upon request.

573 **Methods References**

- 574 44. Koelemeijer, R. B. a., Stammes, P., Hovenier, J. W. & de Haan, J. F. A fast method for
575 retrieval of cloud parameters using oxygen A band measurements from the Global
576 Ozone Monitoring Experiment. *J. Geophys. Res.* **106**, 3475 (2001).
- 577 45. Stammes, P. *et al.* Effective cloud fractions from the Ozone Monitoring Instrument:
578 Theoretical framework and validation. *J. Geophys. Res. Atmos.* **113**, 1–12 (2008).
- 579 46. Joiner, J. *et al.* The seasonal cycle of satellite chlorophyll fluorescence observations
580 and its relationship to vegetation phenology and ecosystem atmosphere carbon
581 exchange. *Remote Sens. Environ.* **152**, 375–391 (2014).
- 582 47. Joiner, J. *et al.* Filling-in of near-infrared solar lines by terrestrial fluorescence and
583 other geophysical effects: Simulations and space-based observations from
584 SCIAMACHY and GOSAT. *Atmos. Meas. Tech.* **5**, 809–829 (2012).
- 585 48. Lee, J. *et al.* Forest productivity and water stress in Amazonia : observations from
586 GOSAT chlorophyll fluorescence Forest productivity and water stress in Amazonia :
587 observations from GOSAT chlorophyll fluorescence. *Proc. R. Soc. B* **280**, 20130171
588 (2013).
- 589 49. Duveiller, G. & Cescatti, A. Spatially downscaling sun-induced chlorophyll
590 fluorescence leads to an improved temporal correlation with gross primary
591 productivity. *Remote Sens. Environ.* **182**, 72–89 (2016).
- 592 50. Guanter, L. *et al.* Retrieval and global assessment of terrestrial chlorophyll
593 fluorescence from GOSAT space measurements. *Remote Sens. Environ.* **121**, 236–251
594 (2012).
- 595 51. Guanter, L. *et al.* Global and time-resolved monitoring of crop photosynthesis with

- 596 chlorophyll fluorescence. *Proc. Natl. Acad. Sci. U. S. A.* **111**, E1327-33 (2014).
- 597 52. Yang, X., Tang, J., Mustard, J. F., Lee, J. & Rossini, M. Solar-induced chlorophyll
598 fluorescence correlates with canopy photosynthesis on diurnal and seasonal scales in a
599 temperate deciduous forest. **42**, 2977–2987 (2015).
- 600 53. Anav, A. *et al.* Reviews of Geophysics primary production : A review. *Rev. Geophys.*
601 787–818 (2015).
- 602 54. Jung, M. *et al.* Global patterns of land-atmosphere fluxes of carbon dioxide, latent
603 heat, and sensible heat derived from eddy covariance, satellite, and meteorological
604 observations. *J. Geophys. Res.* **116**, G00J07 (2011).
- 605 55. Xu, L. *et al.* Satellite observation of tropical forest seasonality: spatial patterns of
606 carbon exchange in Amazonia. *Environ. Res. Lett.* **10**, 84005 (2015).
- 607 56. Parazoo, N. C. *et al.* Interpreting seasonal changes in the carbon balance of southern
608 Amazonia using measurements of XCO₂ and chlorophyll fluorescence from GOSAT.
609 *Geophys. Res. Lett.* **40**, 2829–2833 (2013).
- 610 57. Granger, C. W. J. Testing for causality. A personal viewpoint. *J. Econ. Dyn. Control* **2**,
611 329–352 (1980).
- 612 58. Taylor, K. E., Stouffer, R. J. & Meehl, G. A. An overview of CMIP5 and the
613 experiment design. *Bull. Am. Meteorol. Soc.* **93**, 485–498 (2012).



aPrecip \rightarrow SIF \rightarrow Precip**b**PAR \rightarrow SIF \rightarrow PAR

-0.3

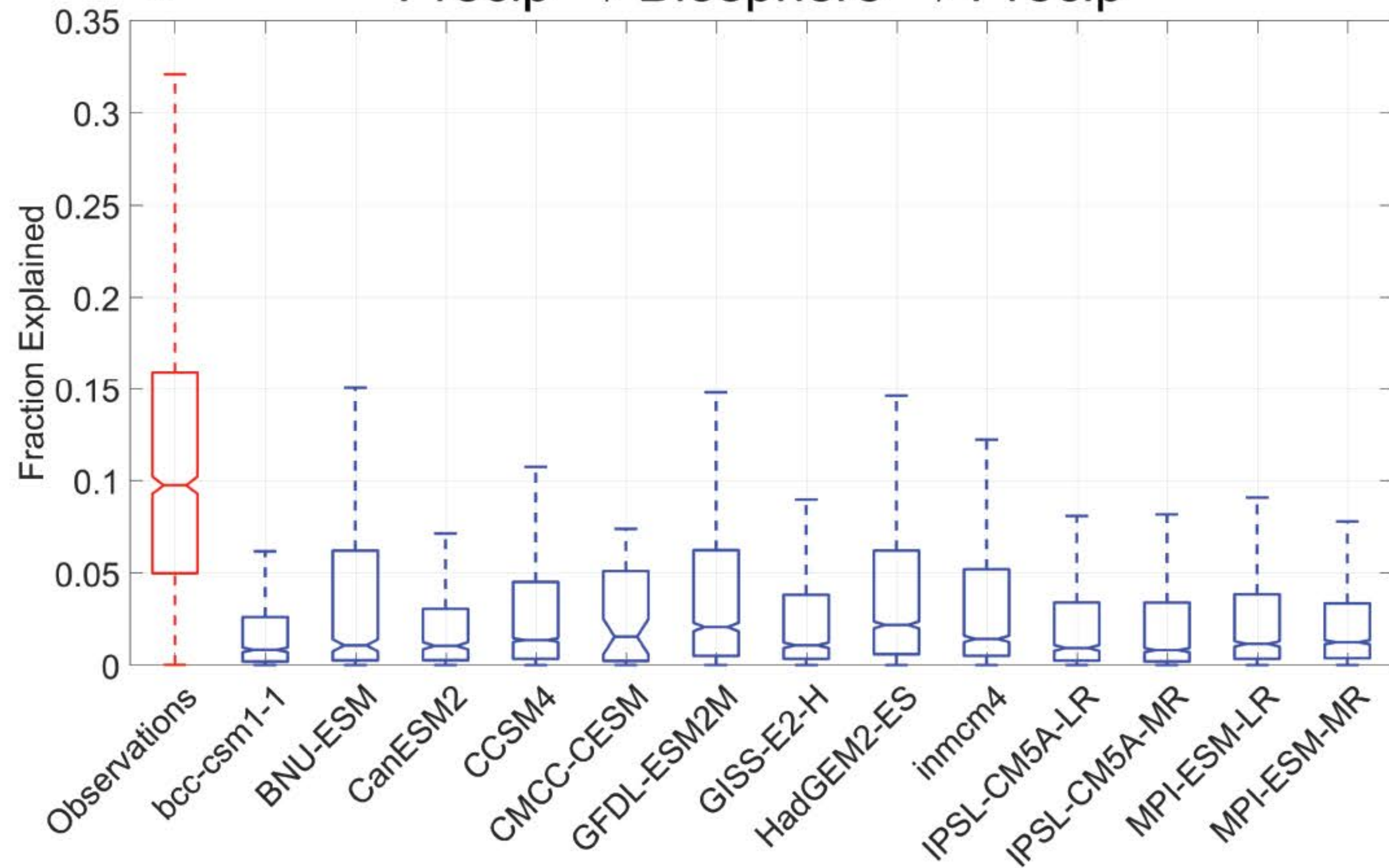
-0.18

-0.06

0.06

0.18

0.3

aPrecip \rightarrow Biosphere \rightarrow Precip**b**PAR \rightarrow Biosphere \rightarrow PAR